Supplemental Materials for Small-Scale, Long-Duration, and Biodegradable Zinc-Air Batteries

Jingwen Zhang and Mark G. Allen

Department of Electrical and Systems Engineering, University of Pennsylvania, USA

Wax material selection

Table S1 shows a summary of the composition and physical properties of natural waxes and petroleum-based wax. Wax hardness is defined by the peak force (g) generated by a cylindrical probe penetrating into wax for a fixed distance(5 mm) under a specific test speed (0.2 mm/s) [1]. The shorter the distance, the harder the wax is. The cohesiveness of wax is the tendency of a material to cohere or hold together, due to intermolecular attraction [2]. It is measured by a compression test or three-point bending test, with the force-distance curve plotted, and the area under the curve is defined as wax cohesiveness (g.mm) [3]. The lower the cohesiveness, the more brittle the material. A mixture of beeswax and soy wax (3:1 in mass) is selected to achieve both high hardness and high cohesiveness for battery encapsulation. The addition of soy wax in beeswax potentially increases the overall hardness at the cost of cohesiveness.

Table S1 Summary of Waxes Composition and Physical Properties [4].

Material	Components	Hardness	Cohesiveness	Melting Temperature	References
Commercial paraffin	Mainly linear hydrocarbons (C20-40)	High ~ 6700 g	Medium ~8000 g.mm	Medium ~ 65 ℃	[1]
Beeswax	Hydrocarbons, fatty acids and long-chain esters	Medium ~ 3500 g	Very high ~ 40,000 g.mm	Medium ~ 65 ℃	[1,5–7]
Carnauba wax	Hydrocarbons, aliphatic and aromatic esters	Very high ~ 60,000 g	Low ~ 2000 g.mm	High ~ 84 ℃	[8,9]
Soywax	Fatty acids and glycerol	Medium ~ 4000 g	High ~ 18,000 g.mm	Low ~ 50 ℃	[1]

Apart from the mechanical and barrier properties, the degradation behavior of the package must also be considered. A biodegradable material with a relatively short degradation time is more prone to dispersion in the environment if fully degraded. One approach to alter the functional and physical properties of natural waxes is by mixing them to form binary systems [10]. For instance, a blend of beeswax and soy wax has been utilized as soil-degradable hydrophobic encapsulants for soil moisture sensors with a tunable degradation period, as reported by Sui et al. [11,12]. These waxes protect the sensor for months of functional lifetime in soil and degrade at a faster rate compared to pure Beeswax. Simultaneous ecotoxicity tests suggested that these waxes do not hinder the growth of maize. Moreover, both beeswax and soy wax are solid at room temperature and have a relatively low melting temperature, making them easy to reshape. Therefore, a mixture of beeswax and soy wax was chosen as the packaging material for the subsequent study.

Neutral gel fabrication

As described in the materials and methods section in the main manuscript, the neutral gel is prepared by forming a precursor from PVA and ionic solutions, casting onto a Petri dish, and undergoing a series of freeze-thaw cycles to promote the formation of the desired gel mechanical properties. Figure S1 shows the various stages of this process, from casting on the Petri dish to the final gel, and qualitatively describes the state of the gel after each thaw cycle.

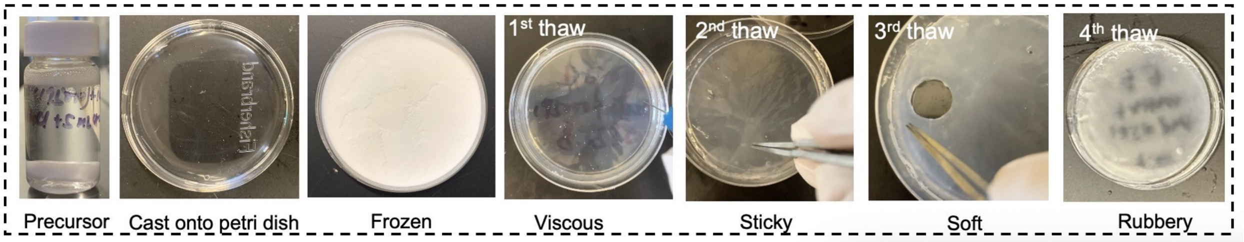

Figure S1 Photo of the neutral gel precursor and the freeze-thaw process of the neutral gel on Petri dishes

Preparation of the molds for wax pad fabrication

Molds for the wax package were prepared from PDMS; however, the PDMS molds themselves were prepared as described here. First, Plexiglas boards (3 mm thick) were laser cut using a CO_2 machining laser into a square piece (20x20 mm^2) and two hollow square pieces (30x30 mm^2, 2 mm wide). The square piece was first glued on a glass substrate using water-soluble school glue, a hollow square piece was then glued concentrically on the same substrate. The second hollow square piece was aligned and glued on top of the first hollow square piece to thicken the outer wall, as shown in Figure S2 to form the first mold. Silicone Elastomer was purchased (SYLGARD 184 Silicone Elastomer Kit, Ellsworth Adhesives) and used to cast into this Plexiglas mold. Part A (pre-polymer) and part B (curing agent) were mixed at a mass ratio of 10:1 by manually stirring for 5 mins in the ambient environment. This PDMS precursor was then desiccated in a vacuum oven at -760 torr (the vacuum pump was turned on until the vacuum level nominally reached -760 Torr; then the pump was turned off and the vacuum was held at this level) at 20 ℃ until all bubbles are removed. The PDMS precursor was then poured into the Plexiglas mold and was placed back into the vacuum oven at -760 torr for approximately 20 mins to remove any trapped air bubbles. After degassing, the PDMS-bearing mold was placed in an oven to be cured at 80 ℃ overnight. The cured PDMS was carefully demolded from the mold under tap water (to assist removal of the school glue), resulting in the PDMS mold used for subsequent wax package preparation.

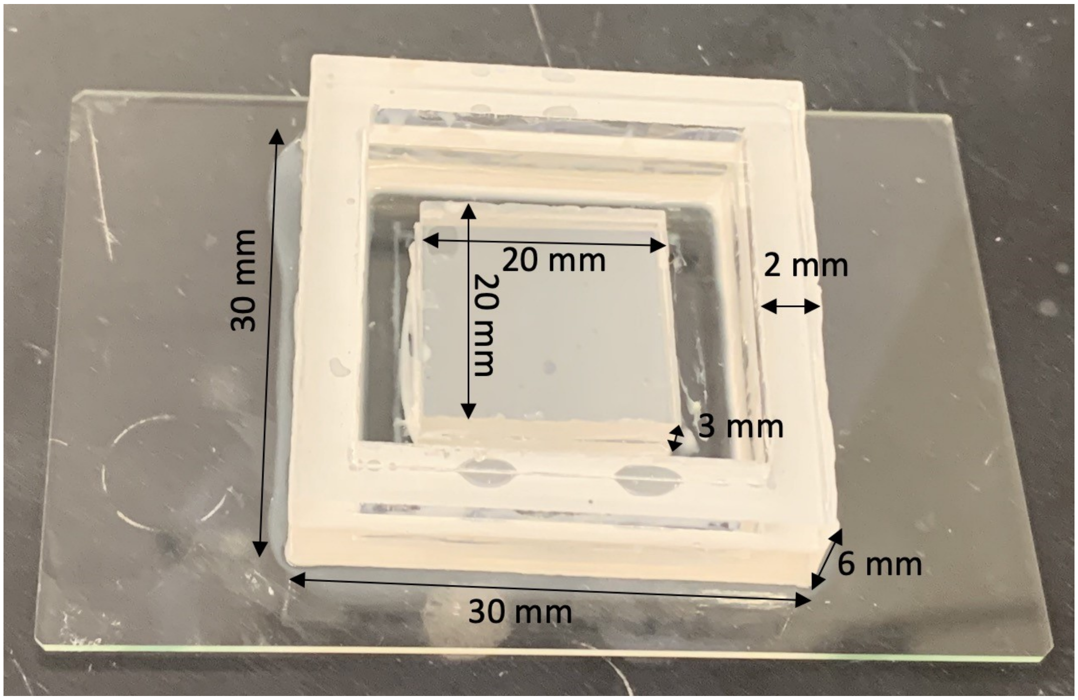

Figure S2 Photo of the mold built by gluing laser-cut Plexiglas boards on a glass substrate at a tilted angle.

Wax-encapsulated battery assembly:

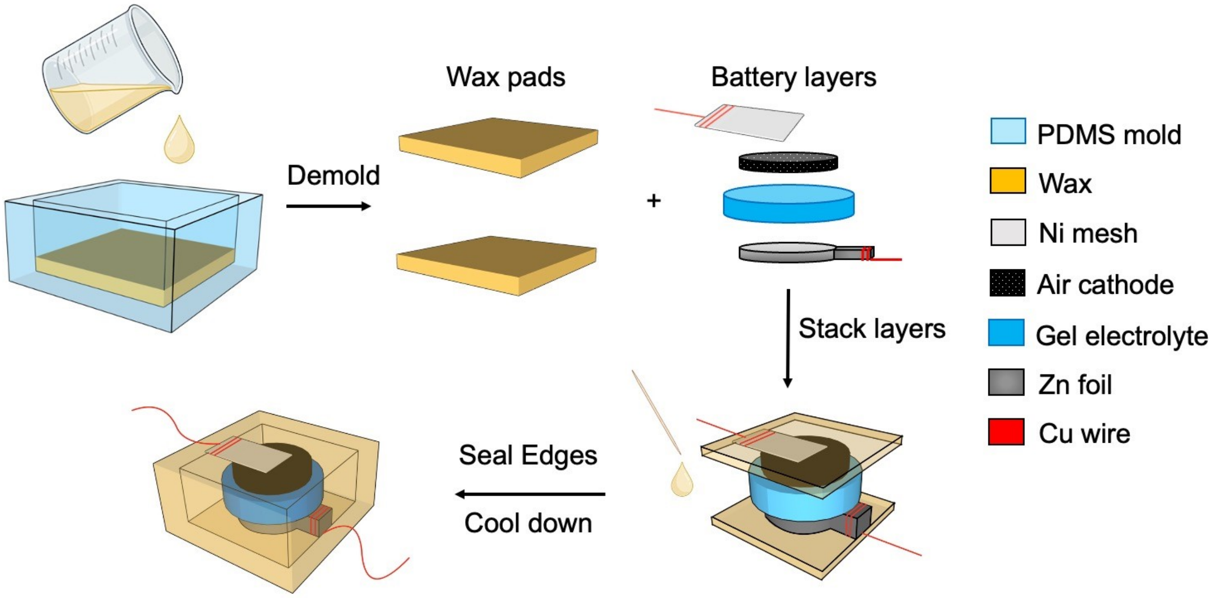

Figure S3 Schematic view of the wax-encapsulated battery fabrication process.

To enhance the wax package, for some batteries, after sealing the edges manually, the battery as a whole was lifted by holding the two Cu wire leads and then immersed in a molten wax mixture (beeswax:soy wax=3:1, melted under 80 °C) for approximately 5 seconds. The battery was then pulled out from molten wax in 1 second and cooled at room temperature to form an additional conformal layer of wax on the outside of the previously-encapsulated battery.

Batteries with and without Loctite sealing

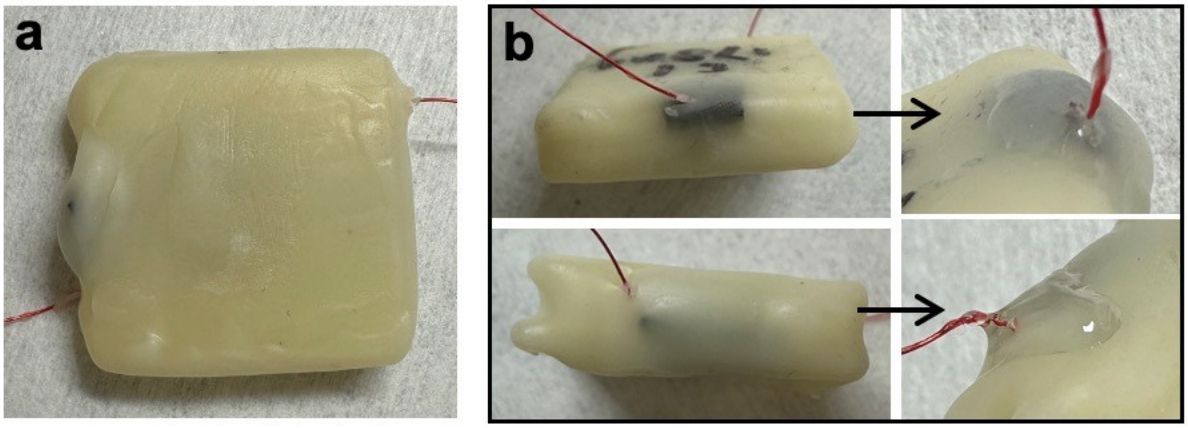

Figure S4 Images of (a) a battery without Loctite (top-down view), and (b) a battery with Loctite sealing the potential air paths around the Cu wires (edge view).

Battery Internal Oxygen Level During Discharge

The battery package comprises an initial volume of air (containing oxygen), together with electrochemically active materials (anode, electrolyte, cathode), and mass transport means to replenish the oxygen in the package that is consumed during battery discharge. To assess the relationship between the oxygen level in the package and the electrochemical performance of the battery (such as output voltage), the internal oxygen level of the battery was examined under different discharge loads. Conceptually, the approach taken was to incorporate a small oxygen sensor within the battery volume. A needle-type optical oxygen microsensor (NTH-PSt7, PreSens Precision Sensing) was used to measure the oxygen level as shown in Figure S5 (a). This sensor has an oxygen-sensitive optical fiber tip, mounted inside a stainless steel needle. The needle was inserted inside the wax package close to the battery’s cathode, where oxygen is consumed. This sensor outputs a normalized oxygen level, in which a reading of 100% corresponds to an absolute oxygen percentage in air of 21%.

To assemble a battery with the oxygen sensor tip encapsulated, a customized procedure was developed. The battery's electrochemical active components include carbon cathode (Sigracet 22 BB), alkaline gel (PVA-KOH-K_2CO_3 gel), Zn anode, and Ni mesh current collector. These battery electrochemical active layers were stacked on a wax pad. A flask rubber stopper was shaped into a cuboid with a thickness comparable to that of the electrochemical active layers of the battery. This stopper piece was used as a rubber spacer to immobilize the metal needle of the oxygen sensor, which was inserted through this rubber spacer. The sensor needle with the rubber spacer was then placed next to the battery cathode. Another wax pad was then placed on top of the electrochemical active layers of the battery and the rubber spacer. A gentle pressure was applied on the top wax pad, and the four edges of two wax pads were paint-sealed with melted wax. Figure S5 (b) shows the internal construction of the battery, with the top wax pad removed for inspection.

The oxygen level was continuously monitored while the battery was discharged and rested (i.e., held under open circuit conditions). The battery was discharged under a sequential constant current load (30 μA-150 μA-330 μA-1 mA-2 mA-5 mA-10 mA). For each current load, the battery was discharged for 15 mins to enable it to reach a plateau oxygen concentration value. The battery was then rested for 30 mins allowing oxygen to refill the package (note that the oxygen level recovered to 100% within 30 mins).

Figure S5 (c) and (d) show the discharge curve and the corresponding oxygen level as a function of time, parameterized by load currents. For each load current, the current draw was initiated at time t=0 min. In general, it was observed that as the discharge load current increased, both the voltage during discharge as well as the oxygen level in the package decreased. For 5 mA and 10 mA load currents, the voltage of the battery during discharge was highest at the beginning of the discharge, dropped gradually, and then plateaued over time. Meanwhile, the oxygen level inside the wax package decreased continuously and plateaued at a similar time point as the voltage profile, implying that the low working voltage of the battery can be attributed to the low concentration of oxygen inside of the wax package, especially under high discharge rate (oxygen consumption rate). The plateau voltage of the battery as a function of the internal oxygen level can be extracted from correlating the data in Figures S5 (c) and (d), and is presented in Figure S5 (e).

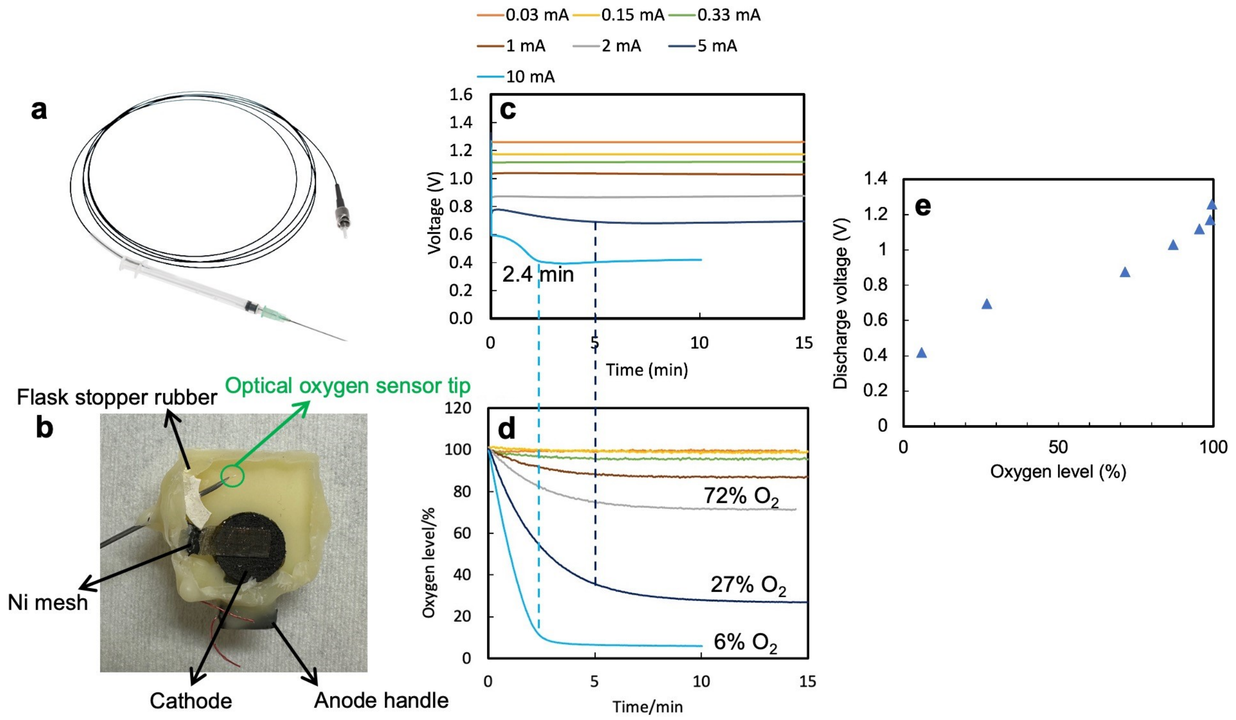

Figure S5 (a) Photo of a needle-type optical oxygen microsensor (NTH-PSt7), (b) photo of the internal construction of a battery with the optical oxygen microsensor tip inserted to monitor the internal oxygen level while discharging, the top wax pad was removed for the visualization, (c) the discharge profiles of the battery under different current loads, (d) the corresponding oxygen level inside the battery under different current loads, and (e) the plateau voltage as a function of the oxygen level inside the wax package.

Water uptake of the gel in the wax package

Gels of approximately 300 mg mass were encapsulated in the wax package following the battery assembly process without anode, and with or without cathode, as shown in Figure S6 (a), (b) and (c). Gels were taken out of the rehydration solution, a textile wipe was used to gently remove the liquid on the surface, and the gel was weighed to obtain the initial gel mass immediately before the encapsulation. After wax encapsulation the gels were stored in the ambient air for 79 days. The wax packages were then carefully opened and the gels were taken out and weighed to calculate the mass loss. The images of both sides of the gel after weigh can be seen in Figure S6 (d)-(i)

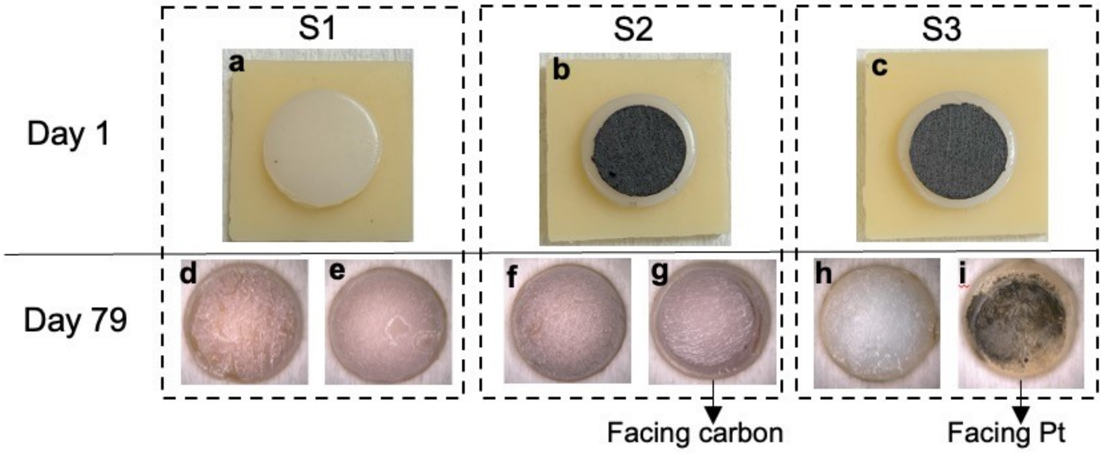

Figure S6 (a), (b), and (c) are top views of a piece of gel lying on top of a wax pad without a cathode, with a carbon cathode (Sigracet 22 BB), and with a Pt-loaded cathode right before the encapsulation. (d), (f) and (h) are images of the gel facing the wax pad after encapsulated in wax package and stored in the ambient air for 79 days. (e), (g) and (i) are images of the other side of the gel facing the wax pad, carbon cathode, and Pt-loaded cathode on day 79.

Table S2 Summary of mass loss of gels in wax packages.

Sample	cathode	Day-1 mass/mg	Day-79 mass/mg	Mass loss ratio
S1	/	300	275.8	8.1%
S2	Sigracet 22 BB	308.5	249.8	19%
S3	Pt-loaded cathode	307.5	265.5	13.7%

Carbon cathode performance under various current loads

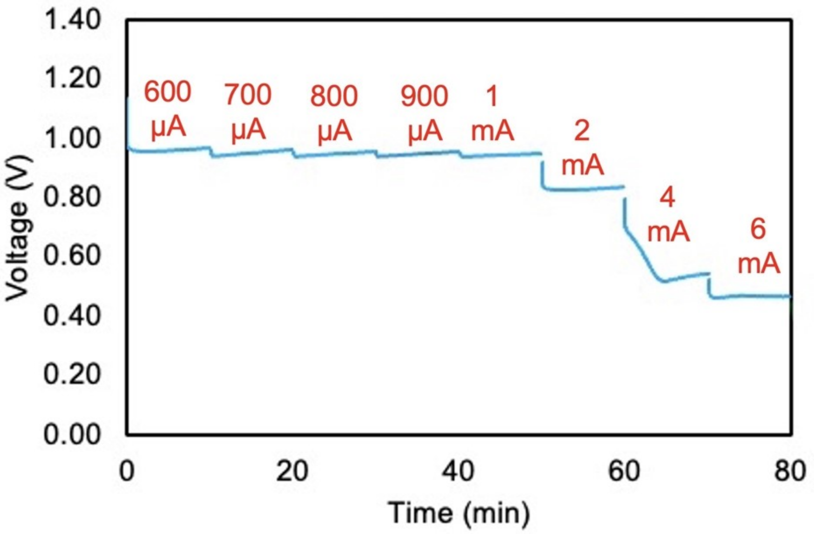

Figure S7 Multi-step discharge profile with 600 µA – 8 mA current load of a battery with Sigracet 22BB in the air, assembled using clamp boards

Higher discharge currents of 600 µA – 8 mA were utilized when characterizing the carbon paper cathodes to understand their catalytic performance in the absence of Pt. Figure S7 shows the multi-step discharge profile of the battery, which has approximately 1 V output voltage when operating at current loads smaller than 1 mA, illustrating that the carbon cathode alone has sufficient catalytic activity for IoT sensor applications even at higher discharge rates.

Corrosion current characterization

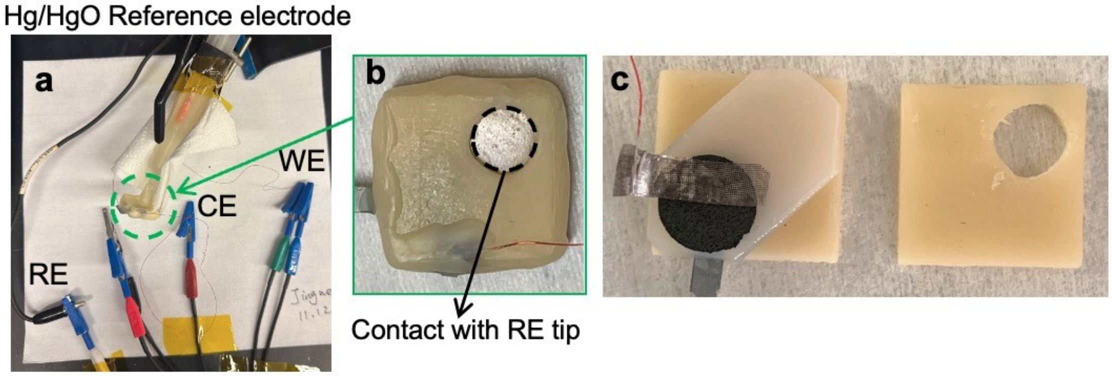

Figure S8 (a) Three-electrode corrosion current characterization set-up, (b) top view of the battery, (c) internal components of the battery.

Figure S8 (a) shows the corrosion test experimental setup with a three-electrode construction. A mercury/mercury oxide (Hg/HgO) reference electrode (RE) was used with the tip contacting the hydrogel of the battery through a hole opened on the wax pad as shown in Figure S8 (b) and (c). Internally, the Zn anode (in the shape of a 1 cm diameter disc with a rectangular handle) with or without PEG 600 and Tween 20 was placed close to the corner of the wax pad as the working electrode (WE). An extended piece of hydrogel with or without MLD and a Pt-loaded carbon paper cathode were stacked on top of the anode to form a full cell, with the cathode connected as the counter electrode (CE).

A small polarized potential E was applied away from the equilibrium of the battery E_{corr}, and the corresponding current level i was then collected. The relationship between potential and current can be described by the Butler-Volmer equation (Equation 1), where $i_{corr}, F, n, T, and\ R$ are internal exchange current density, Faraday constant, number of the electrons involved in the reaction, absolute temperature, and ideal gas constant.

$$i = i_{corr}\exp\left[\frac{\alpha nF\eta}{RT}\right] - i_{corr}\exp\left[\frac{-(1-\alpha)nF\eta}{RT}\right] \tag{1}$$

$\eta = E - E_{corr}$

Gamry Echem Analyst was used to conduct a multi-variable numerical fit to extract the values of corrosion current and corrosion potential from the polarization curves.

Alkaline gel degradation over long-term discharge

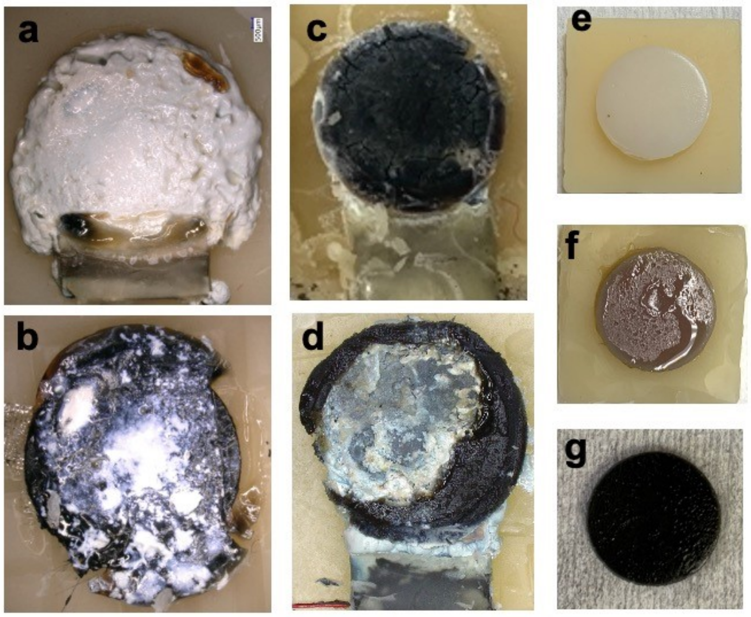

Figure S9 Optical images of (a) the Zn anode (the side facing the hydrogel), (b) hydrogel after discharge on top of the cathode of the battery discharged for 70 days in the air; (c) hydrogel after discharge on top of the anode of the battery discharged for 50 days in the soil; (d) a disintegrated hydrogel on top of the Zn anode of a discharged battery; hydrogel disc on top of a wax pad (e) before assembly, (f) after encapsulated in the wax package with carbon paper cathode placing on top for about 2.5 months, (g) after storing the hydrogel in the alkaline rehydration solution for 1 year 9 months.

Gels stored for long periods of time (many months) in a high-pH solution such as the alkaline rehydration solution exhibited discoloration (Figure S9 (g)) as described in the main text. Apart from the discoloration, another degradation phenomenon was observed only for the gels assembled into batteries and discharged for more than a few weeks. This was gel disintegration, where the hydrogel did not hold its original disc shape, but instead broke into smaller pieces or turned into a dark brown thick liquid as shown in Figure S9 (d). As the Zn-air battery discharges, the Zn ion can diffuse into the hydrogel as deep as 500 μm, which may also increase as the discharge time increases, which may lead to a change in the membrane structure [13]. The mechanical properties of the hydrogel may also be changed due to the intermolecular hydrogen bonds formed between the O-H groups of PVA and the ZnO as the ZnO nucleates within the gel [14]. Considering that the hydrogel electrolyte provides the ionic conductive path within the battery, its degradation may also lead to the end of the discharge of the battery.

Comparison with state-of-the-art biodegradable primary batteries

Table S3

Data sources	Average discharge power (uW/cm^2)	Discharge current density (uA/cm^2)	Lifetime (days)	Working voltage (V)	Note
Our work	45.9	38.2	71.9	1.2	Large cell in the air
Our work	47.8	38.2	49.2	1.25	Large cell in soil
Our work	1.9	38.2 (5% duty cycle)	260	1	Large cell in soil
Our work	1.9	38.2 (5% duty cycle)	340	1	Large cell in the air
Our work	5.0	71.4 (5% duty cycle)	82.3	1.18	corn cell in the air
Our work	4.8	71.4 (5% duty cycle)	65.5	1.15	corn cell in the soil
[5]*	250.0	400.0	3.75	0.625	
[60]*	3.5	5.0	19	0.7	
[61]*	18.8	25.0	13	0.75	
[62]*	108.0	600.0	7	0.18	

* Reference numbers listed in this table are taken from the main text.

Summary plot (Figure 9(d)) source data of our work

Table S4

Data sources	Working voltage (V)	Discharge current density (uA/cm^2)
Our work	0.95	764.3
Our work	0.95	891.7
Our work	0.95	1019.1
Our work	0.95	1146.5
Our work	0.94	1273.9
Our work	0.82	2547.8

References

1. Yao, L., Lio, J., Wang, T. & Jarboe, D. H. Synthesis and characterization of acetylated and stearylyzed soy wax. *JAOCS, Journal of the American Oil Chemists' Society* **90**, (2013).

2. Stable micro systems. How to measure cohesiveness. *https://www.stablemicrosystems.com/MeasureCohesiveness.html*.

3. Yao, L. & Wang, T. Textural and physical properties of biorenewable 'waxes' Containing partial acylglycerides. *JAOCS, Journal of the American Oil Chemists' Society* **89**, (2012).

4. Fei, T. & Wang, T. A review of recent development of sustainable waxes derived from vegetable oils. *Current Opinion in Food Science* vol. 16 Preprint at https://doi.org/10.1016/j.cofs.2017.06.006 (2017).

5. Tulloch, A. P. Beeswax—Composition and Analysis. *Bee World* **61**, (1980).

6. Tulloch, A. P. The composition of beeswax and other waxes secreted by insects. *Lipids* **5**, (1970).

7. Ribas Garriga, M. Evaluation of natural wax for green packaging applications. *Department of Engineering Sciences and Mathematics* **1**, (2019).

8. Moravej, M., Prima, F., Fiset, M. & Mantovani, D. Electroformed iron as new biomaterial for degradable stents: Development process and structure–properties relationship. *Acta Biomater* **6**, 1726–1735 (2010).

9. Basson, I. & Reynhardt, E. C. An investigation of the structures and molecular dynamics of natural waxes. II. Carnauba wax. *J Phys D Appl Phys* **21**, (1988).

10. Jana, S. & Martini, S. Phase Behavior of Binary Blends of Four Different Waxes. *JAOCS, Journal of the American Oil Chemists' Society* **93**, (2016).

11. Sui, Y. *et al.* Controlled Biodegradation of an Additively Fabricated Capacitive Soil Moisture Sensor. *ACS Sustain Chem Eng* **9**, (2021).

12. Atreya, M. *et al.* Wax Blends as Tunable Encapsulants for Soil-Degradable Electronics. *ACS Appl Electron Mater* **4**, (2022).

13. Santos, F., Tafur, J. P., Abad, J. & Fernández Romero, A. J. Structural modifications and ionic transport of PVA-KOH hydrogels applied in Zn/Air batteries. *Journal of Electroanalytical Chemistry* **850**, (2019).

14. Asadpour, S., Raeisi vanani, A., Kooravand, M. & Asfaram, A. A review on zinc oxide/poly(vinyl alcohol) nanocomposites: Synthesis, characterization and applications. *Journal of Cleaner Production* vol. 362 Preprint at https://doi.org/10.1016/j.jclepro.2022.132297 (2022).